Texture Analysis of Seabed Images to Quantify the Presence of *Posidonia Oceanica* Using Logistic Model Trees

Miguel F. Massot Campos
and
Gabriel Oliver Codina
Systems, Robotics and Vision Group
Universitat de les Illes Balears

An automatic classifier algorithm has been designed to assess the population of *Posidonia Oceanica* over a set of underwater images taken at Palma Bay. Laws' energy filters and statistical descriptors of the Gray Level Co-occurrence Matrix have been used to correctly classify the input image patches in two classes: *Posidonia Oceanica* or not *Posidonia Oceanica*. The input images have been first preprocessed and splitted in three different patch sizes in order to find the patch size to classify this seagrass. From all the attributes obtained in these patches, a best subset algorithm has been run to choose the optimal set of attributes. Then a decision tree classifier has been trained. The classifier was made by training a Logistic Model Tree from 125 pre-classified images. This classifier was finally tested on 100 new images. The classifier outputs gray level images where black color indicates *Posidonia Oceanica* presence and white no presence. Intermediate values are obtained by overlapping the processed patches, resulting in a smoother final result. This images can be merged in an offline process to obtain population density maps.

Keywords: Image processing, Texture analysis, Data mining, Underwater robotics

1. INTRODUCTION

Posidonia Oceanica (PO) is an endemic seagrass specie of the Mediterranean sea that forms large meadows on seabeds up to $40\ m$ deep. The presence of PO is very important to the underwater ecosystem and to the industry developed in the coastal areas, specially tourism and fishing activity, because its profusion is strongly related to biodiversity and water quality of the environment. Unfortunately, the habitat of PO is declining due to anthropogenic impacts (eutrophication, uncontrolled anchoring, trawling, shoreline change) [González-Correa et al. 2005] and large-scale changes (increased temperature, biological invasions, among others) [Diaz-Almela et al. 2007]. Because of its slow growth and recovery, losses may be irreversible. Thus, regular mapping of PO communities plays an important role in its conservation monitoring [Ardizzone et al. 2006; Scaradozzi et al. 2009].

Traditionally, scuba divers in a process that is dangerous, slow, tedious, expensive and imprecise, carry out the abovementioned survey task. More recent technologies, using sensorized and equipped structures [Piazzi et al. 2000; Matarrese and Acquaro 2008; Siccardi et al. 1997] or even from satellites [Pasqualini et al. 2005], overcome these problems. One of these platforms has been developed by the *Instituto Mediterráneo de Estudios Avanzados* (IMEDEA) in the last years [March et al. 2013]. This underwater platform is equipped so it can take images at a fixed distance from the seabed and with almost similar illumination conditions. Moreover, the images are located using the GPS data of the supply boat from where the platform is being deployed. Using this system, more than 3.000 georeferenced images (some samples are shown in figure 1), were taken in Palma Bay Marine Reserve (Mallorca, ES) in 2009. These images were taken at different times and places, as depicted in figure 2. They do not correspond to a continuous survey or film.

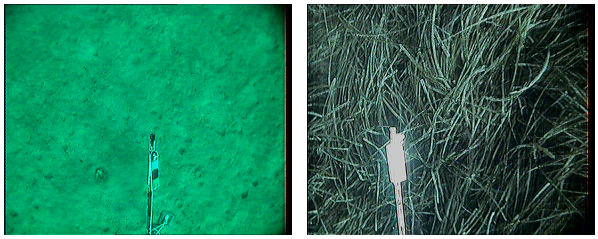

(a) No posidonia present, all sand. (b) All posidonia.

Fig. 1. Extract of photos.

Palma Bay Marine Reserve (PBMR) is delimited by the intersection of the coast with the parallel 39º28.6'N and 39º27.03'N, and up to 30 m depth. Inside this area there is a 2 km^2 Integral Zone (IZ) area where all extractive activity or anchoring on the PO prairies is forbidden, whilst in the rest PBMR lower fishing is allowed. The reserve was founded with the objective of increasing the natural resource regeneration and conserve representative ecosystems. This scenario is the key to compare different PO communities growth inside and outside the boundaries of the reserve. More information on these images and on the site can be found in [March et al. 2013].

Remotely Operated Vehicles (ROVs) have already been used to achieve this task [Matarrese and Acquaro 2008]. Thus, the next technological step would be to use Autonomous Underwater Vehicles (AUVs) carrying the operation of surveying and classifying the incoming data in their corresponding class or label. With as little as an onboard camera and the needed thrusters to move, even a simple robot could overcome the scuba divers problems above mentioned.

The motivation of this work is to provide an automatic way to assess the presence of PO in the mentioned images. Thanks to that, the monitoring process can be extended to consider denser sam-

This work has been partially supported by the Spanish Ministry of Education (FPI grant BES-2012-054352), the Balear Goverment (ref 71/2011), FEDER funds and by the Spanish Ministry of Research and Innovation DPI2011-27977-C03 (TRITON Project).
Author address: miquel.massot@uib.cat.

Màster Universitari en Tecnologies de la Informació (MTIN)
http://postgrau.uib.cat/es/master/MTIN/

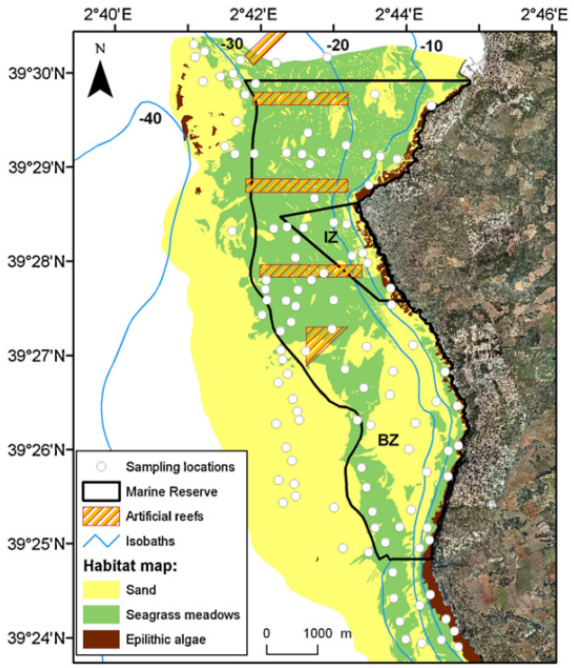

Fig. 2. Map of the study area showing the sampled locations. Palma Bay Marine Reserve (PBMR) boundaries enclose the Integral Zone (IZ) and the Buffer Zone (BZ). The location of the zones of artificial reefs in PBMR are presented. From [March et al. 2013].

pling of the PO meadows and longer temporal series. Thus, map generation [Fornes et al. 2006] and recovery studies [González-Correa et al. 2005] could be guided by the results of our proposal.

This work is presented as follows: in section 2 the input image characteristics are presented, and the image preprocessing is explained detailing how the images are labelled for posterior training. There, the different obtainable attributes from the Laws' Texture Energy Measurements and the Grey Level Co-occurence matrix are presented. In section 3 the best suited classifier is chosen, logistic model trees in the case of this study, then the most suitable attributes are chosen following a best subset selection criteria to finally train the model, which is tested in section 4. Finally, in section 5 conclusions and further work are presented.

2. PREPROCESS

The images used in this study were provided by IMEDEA, and were captured using a analogic RGB camera housed in a watertight case. The original image size is 720×576 pixel and presents vignetting and a color calibration pattern that was physically placed when the photos were taken (see figure 4). Even with the presence of the color calibration pattern, the photographs lack a correct color balance and contrast. Moreover, to prevent possible errors in the algorithms caused by the presence of the calibration pattern, the process has been restricted to the higher part of the image. This restriction is made to avoid the external elements interference in the image processing and in the classifier training processes.

Finally, the useful resolution of the images became 650×300 pixels. The preprocess involves also the conversion of the input photos to black and white. For instance, the resultant preprocess of image 3 is image 5, where in 4 is shown the region of interest.

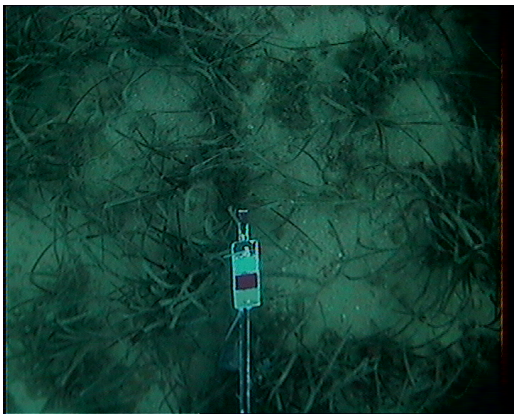

Fig. 3. Original size input image. Note the color calibration pattern and the plumb, as well as the left and right black frame and the vignetting.

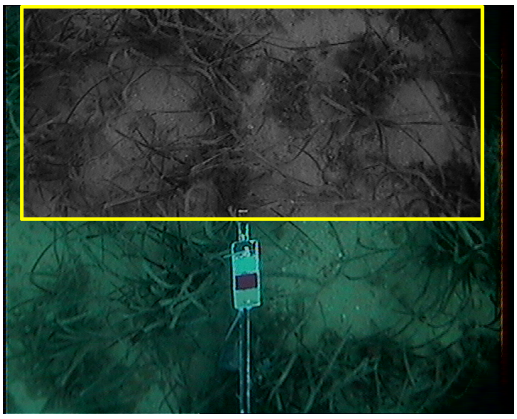

Fig. 4. Region of interest of the original image. The top, left and right borders have been also removed to reduce vignetting. The bottom part where the calibration pattern usually appears has been totaly removed.

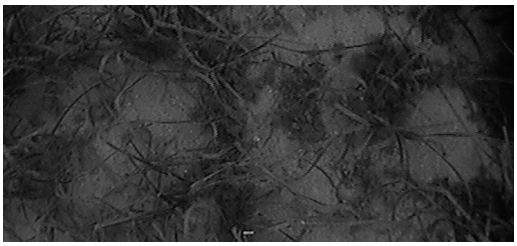

Fig. 5. Preprocessed input image. The image is converted to black and white because the color information of the images is not relevant for the classification process.

Next, each image is split in several non-overlapping subimages or patches. These subimages are later used to calculate several values to train the classifier. As the optimal size of the subimage is not known, three different sizes have been chosen and all three will be tested, using them to train three different classifiers. The size of these subimages has been chosen to be 25×25, 50×50 and 75×75 pixels, generating three different subimage databases. Some patches can be seen in figure 6. These sets will be referenced from now on as A, B and C. Note that the A set will have more examples

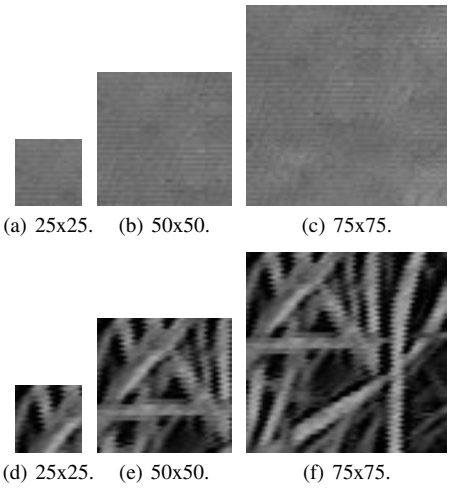

(a) 25x25. (b) 50x50. (c) 75x75.

(d) 25x25. (e) 50x50. (f) 75x75.

Fig. 6. Sand and posidonia patch sizes.

than the C because the amount of 75×75 subimages present in one whole image is lower than the number of 25×25 subimages.

In order to describe these images, Laws' Texture Energy Measurements and Grey Level Co-occurrence Matrix [Haralick et al. 1973] will be used to identify the differences in texture. These patches will be classified in a binary class: a patch will be either PO or not PO. In the case of Palma Bay photographs, not PO is sand and little pebbles. The identification of other types of seabed (rocks, other algae) is out of the focus of this work.

As each image is split in subimages, each patch can be classified in one or another class, leading to a resultant global classified image that is not binary. The patches can also overlap, leading to smoother details on the output image. The result classification measure of the whole image is

$$s = \frac{\sum_P k_i}{\sum_{P \cup N} k_i} \tag{1}$$

where k_i is the classification of the i-th patch of the image, P is the subset of patches classified as PO and N is the subset of patches classified as not PO. Note that $P \cup N$ are all the patches in the image. The classification is done at patch level, but the results can be interpreted at both image level and patch level. In section 4 both interpretations are discussed.

2.1 Laws' Texture Energy Measurements

Texture filters like Laws' Texture Energy Measurements (TEM) can be applied to the input images to create filtered images from which texture features are computed.

The Laws' algorithm first filters the input image using texture filters that will be explained later. Then it computes the texture energy by summing the absolute value of filtering results in local neighbourhoods around each pixel. To obtain rotational invariance, two filters can be combined by applying one filter on the other's result.

Laws' texture filters are made from three different vectors convoluted with themselves to create five different new vectors. These vectors are simple feature detectors commonly named as level, edge, spot, wave and ripple. The convolution of these feature detectors with the input images outputs five gray images where, the darker a pixel is, the more sensitive it is to that particular detector.

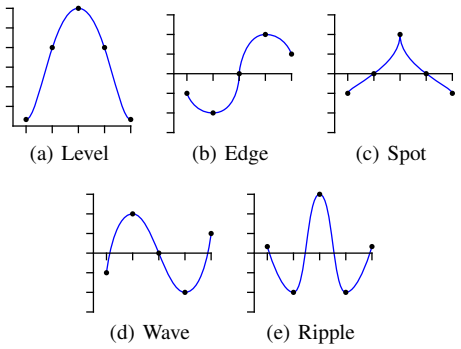

(a) Level (b) Edge (c) Spot

(d) Wave (e) Ripple

Fig. 7. Laws' TEM features searched in the images.

$$\begin{array}{rcl} L_5 & = & [\ 1,\ 4,\ 6,\ 4,\ 1] \quad \text{(Level)} \\ E_5 & = & [-1, -2,\ 0,\ 2,\ 1] \quad \text{(Edge)} \\ S_5 & = & [-1,\ 0,\ 2,\ 0, -1] \quad \text{(Spot)} \\ W_5 & = & [-1,\ 2,\ 0, -2,\ 1] \quad \text{(Wave)} \\ R_5 & = & [\ 1, -4,\ 6, -4,\ 1] \quad \text{(Ripple)} \end{array} \tag{2}$$

L_5 returns a local centred average by convolving the neighbour pixels with a Gaussian, E_5 responds to edges by applying a gradient mask, S_5 responds to spots, W_5 responds to wave-like shapes and R_5 to ripples in the texture. The plot of these features can be seen in figure 7, where the different shapes give an overall idea of how the image value must look like in order to be more responsive to a particular TEM.

Convolving different 5-pixel long vectors, other lengths can be obtained. In this paper, 5 pixel, 9-pixel and 17-pixel have been considered due to the different subimage size. Depending on the size of the texture to study, a determined vector size is preferred. For example, L_9 can be created as stated in equation 3.

$$\begin{array}{rcl} L_9 & = & conv(L_5, L_5) \\ & = & [1, 8, 28, 56, 70, 56, 28, 8, 1] \end{array} \tag{3}$$

Then, if every 1D-vector is multiplied with another one, 25 5×5 kernels or 2D-masks can be obtained ($L_5L_5, L_5E_5, L_5S_5, \ldots$). For instance, matrix (4) looks like a gaussian kernel, with its anchor point centered.

$$L_5L_5 = L_5^T \cdot L_5 = \begin{pmatrix} 1 & 4 & 6 & 4 & 1 \\ 1 & 16 & 24 & 16 & 4 \\ 6 & 24 & 36 & 24 & 6 \\ 4 & 16 & 24 & 16 & 4 \\ 1 & 4 & 6 & 4 & 1 \end{pmatrix} \tag{4}$$

The same procedure is made with 9×9 and 17×17 sizes, obtaining a total of $25 + 25 + 25$ different matrices.

These 75 matrices will be convolved with the subimages. In appendix A the same two patches from figures 6(c) and 6(f) are processed with all the different Laws' TEM to provide better insight. From each of these resulting matrices the average (μ), standard deviation (σ), average of positives (μ^+) and average of negatives (μ^-) are calculated, generating a total of $4 \cdot 75 = 300$ descriptors per subimage. These descriptors are then the input attributes for the classification model that will be explained later.

2.2 Grey Level Co-occurrence Matrix

On the other hand, Grey Level Co-occurrence Matrix (GLCM) is a tabulation of how often different combinations of pixel brightness values (grey levels) occur in an image.

This matrix is calculated as follows: given the number of bins and the co-occurence direction, the image is labelled to its corresponding bin. Then the frequency of each combination of neighbour bin labels is annotated in a matrix whose row index is the reference bin value and the column index is the neighbour bin value.

For instance, given a 4×4 image labeled in 4 bins,

$$\begin{pmatrix} 0 & 0 & 1 & 1 \\ 0 & 0 & 1 & 1 \\ 0 & 2 & 2 & 2 \\ 2 & 2 & 3 & 3 \end{pmatrix} \tag{5}$$

and considering only right direction, two times a zero is left to a zero, two times a zero is left to a one, one time a zero is left to a two, and never a zero is left to a three. This is the first row of its corresponding GLCM.

$$\begin{array}{c|cccc} & 0 & 1 & 2 & 3 \\ \hline 0 & 2 & 2 & 1 & 0 \\ 1 & 0 & 2 & 0 & 0 \\ 2 & 0 & 0 & 3 & 1 \\ 3 & 0 & 0 & 0 & 1 \end{array} \tag{6}$$

Finally, this matrix is normalized to $[0, 1]$ space, transforming it into a close approximation of a probability table. It is only an approximation because the values come from integer values and therefore their values will still be discrete whilst a true probability would require continuous values. The normalization is made by

$$P_{i,j} = \frac{V_{i,j}}{\sum_{i,j=0}^{N-1} V_{i,j}}.$$

where $V_{i,j}$ is the value of the bin (i, j).

GLCM is obtained from each of the subimages by calculating the frequency rate of neighbour pixel values. In this paper, GLCM has been computed considering 8 bins. From that matrix the attributes listed in table I are obtained, generating a total of 17 descriptors per instance.

These basic statistic descriptors give significant information on how the shape of the GLCM is. If this matrix has almost all values in a small neighbourhood means that pixel values are close together, and therefore means that the image contrast is poor and its standard deviation is high. Different configurations exist on these descriptors chosen. What is more interesting is seeing which values will the classifier finally choose as the best ones to classify. To show these differences, two images have been chosen as examples, one containing sand in figure 8(a) and the other containing PO in figure 8(b). The differences between the two GLCM are evident, and easy to identify with these simple statistical attributes.

2.3 Labelling

From the whole set of images, those that only have posidonia have been labeled as class 1, and the images where there's only sand and little pebles have been labeled as class 0. However, there are images that have both posidonia and sand. These images have to be classified manually and then binarized to the corresponding patch size in order to train with them.

Table I. Values calculated for each patch.

Attribute	Formula
Average	$\mu = \frac{1}{NM} \sum_{i,j=0}^{N,M} P_{i,j}$
Variance	$\sigma^2 = \sum_{i,j=0}^{N,M} (P_{i,j} - \mu)^2$
Standard deviation	$\sigma = \sqrt{\sigma^2}$
Contrast	$Con = \sum_{i,j=0}^{N,M} P_{i,j}(i-j)^2$
Entropy	$Ent = \sum_{i,j=0}^{N,M} P_{i,j}(-\ln(P_{i,j}))$
Homogeneity	$Hom = \sum_{i,j=0}^{N,M} \frac{P_{i,j}}{(i-j)^2}$
Angular Second Moment	$ASM = \sum_{i,j=0}^{N,M} P_{i,j}^2$
Energy	$E = \sqrt{(ASM)}$
Skew	$Ske = \sum_{i,j=0}^{N,M} \frac{(P_{i,j}-\mu)^3}{\sigma^3}$
Kurtosis	$Kur = \sum_{i,j=0}^{N,M} \frac{(P_{i,j}-\mu)^4}{\sigma^2}$
Maximum probability	$max_i = \max_{i \in N}(P_{i,j})$
	$max_j = \max_{j \in M}(P_{i,j})$
GLCM Mean	$\mu_i = \sum_{i,j=0}^{N,M} i(P_{i,j})$
	$\mu_j = \sum_{i,j=0}^{N,M} j(P_{i,j})$
GLCM Variance	$\sigma_i^2 = \sum_{i,j=0}^{N,M} P_{i,j}(i-\mu_i)^2$
	$\sigma_j^2 = \sum_{i,j=0}^{N,M} P_{i,j}(j-\mu_j)^2$
GLCM Correlation	$\sigma_{ij}^2 = \sum_{i,j=0}^{N,M} P_{i,j} \frac{(i-\mu_i)(j-\mu_j)}{\sqrt{(\sigma_i^2)(\sigma_j^2)}}$

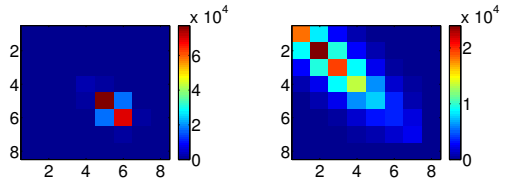

(a) From figure 1(a). (b) From figure 1(b).

Fig. 8. Different GLCM.

As an example, the prior labelling of the mixed image in figure 5 is shown in figure 9(a). This hand-labelled image has been binarized in the tree different patch sizes in order to correctly train the classifier. These three binarized training images can be seen in figure 9.

Some of these mixed images will therefore be not perfectly labeled, due to binarization. Many of them will present both posidonia and sand in the same patch, introducing little errors in the training process.

3. TRAINING

The method proposed to assess the population of PO in an image is based on texture analysis and machine learning algorithms. Several models can be trained from different classifier types (trees, perceptron, Bayes, etc.) In this master thesis, C4.5 decision tree, Logistic Model Tree (LMT), Random forest tree (RF), and Multilayer Perceptron classifiers (MP) have been compared to select the best suited classifier for the task.

The comparison has been made by considering all the attributes in 12 images, six containing PO and six containing sand. The huge number of attributes make the model training to be time consuming. This has been an important reason not to incorporate a large number of images into this training process. These images are used to train the four models using 10 fold cross-validation with Weka

(a) Labeled imaged from figure 5 used to train the classifier.

(b) Binarized labeled image at 25x25.

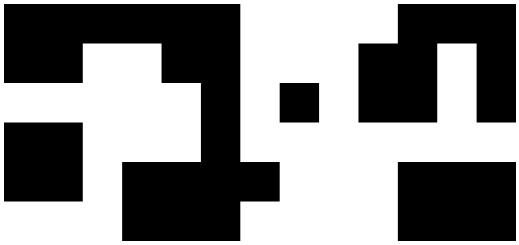

(c) Binarized labeled image at 50x50.

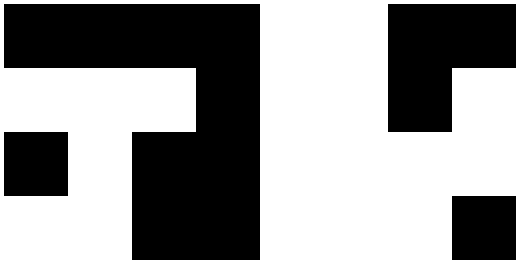

(d) Binarized labeled image at 75x75.

Fig. 9. Hand labeled mixed image and its corersponding binarization depending on subimage size.

[Hall et al. 2009]. This validation method is based on removing a 10% (one fold out of ten) of the training samples to test it later on the model trained with the remaining 90%. Shifting the removed 10% to another location in the training dataset and testing it with the results returns 10 different classifications. The result of the validation is the average of these classification tests.

The labelled images are first preprocessed as stated in Section 2 to obtain a valid text file input for Weka. The best classifier was chosen by selecting the one with the best number of correctly classified instances and the least number of attributes in the three datasets. The different configurations for the models are as follows:

- C4.5 has been trained with a confidence factor of 0.25 and a minimum number of instances per leaf of 2.
- LMT has been trained using the same C4.5 splitting criterion that uses information gain on the class variable and with a minimum number of instances per leaf of 15.
- RF has been trained with 10 trees, unlimited depth and number of attributes to be used.
- MP has been trained by backpropagation with 158 hidden layers, a learning rate of 0.3, a momentum of 0.2 and 500 epochs.

Table II. Correctly classified instances and (number of attributes used).

Classifier	Dataset A	Dataset B	Dataset C
C4.5	98,12% (8)	98,61% (2)	99,54% (1)
Logistic Model Tree	98,71% (7)	99,40% (2)	99,07% (2)
Random Forest	97,02% (2)	95,83% (2)	99,07% (1)
Multilayer Perceptron	98,86% (8)	99,40% (3)	99,07% (2)

The results of these tests are shown in table II. In that table, Random Forest classifier is shown as the classifier that used the least number of attributes, whilst Multilayer Perceptron and C4.5 the ones that used the most. Logistic Model Tree classifier used almost the same number of attributes as Random Forest in datasets B and C, but its classification rate is better than the latter.

Therefore, the work has been focused in one classifier. The Logistic Model Tree (LMT) classifier [Landwehr et al. 2005] has been chosen for its simplicity and good classification rate. With only one classifier, it is easier to find the best subset of attributes for the whole datasets. Although for dataset C, model C4.5 has better classification rate, LMT achieves better rates in A and B datasets, and is also faster classifying than Multilayer Perceptron. Future works could also explore C4.5 in C dataset.

3.1 Logistic Model Tree

This model tree is a combination of a linear logistic regression and decision trees. These trees are built by implementing a logistic regression at their leaf nodes.

The basis of the logistic regression is the logistic function (eq. 7) and its inverse, the logit function (eq. 8).

$$f(\mathbf{X}) = \frac{1}{1+\exp(-\boldsymbol{\beta}\mathbf{X})} \tag{7}$$

$$g(\mathbf{X}) = \ln \frac{f(x)}{1-f(x)} \tag{8}$$

$$= \boldsymbol{\beta}\mathbf{X} \tag{9}$$

$$= \beta_0 + \beta_1 x_1 + \beta_2 x_2 + \cdots + \beta_N x_N \tag{10}$$

where $\mathbf{X} = (1, x_1, x_2, \ldots, x_N)$ are the dependent variables, $\boldsymbol{\beta} = (\beta_0, \beta_1, \beta_2, \ldots, \beta_N)$ are the regression coefficients and N is the number of dependent variables.

Given that the logit function ranges through the interval $(0, 1)$, it provides an adequate criterion to conduct linear regression to a two class variable. Furthermore, it's input extends from $-\infty$ to ∞, which makes it convenient for continuous range input values.

Once the best model has been chosen, the best attribute subset for that model will be determined.

3.2 Selection of the best attributes

The next step is the selection of the best attributes. These attributes have to correctly describe the texture without overfitting the model.

Table III. List of attributes selected as the best subset of LMT classification model.

Attributes selected in	List of attributes
All subsets	Entropy, μ_{L5L5}, μ_{E9L9}, σ_{E5R5}, σ_{R9L9}
Five subsets	σ, μ_{L9L9}, μ_{L17S17}, σ_{E17W17}
Four subsets	$\max_i$, μ_{L17L17}, μ_{L5W5}, μ_{L17W17}, σ_{L9R9}, σ_{E17S17}, μ_{E5W5}, μ_{W5L5}

Six different training datasets have been used to test the different attributes, grouped in pairs. The first three datasets contain 50 full posidonia and 50 full sand images in three subimage sizes. The other three training datasets contain the abovementioned datasets with an addition of 25 mixed sand and posidonia images in the same subimage sizes. These new 25 images have been previously classified and labelled by a human operator. The dataset pairs are then the dataset with or without these 25 new images, which will be referenced as Training set A for the A-sized training set with 100 images, and Training set A' for the A-sized training set with 125 images.

Greedy Stepwise method was used to find the best subset of attributes for a given classifier. This method is based on the greedy algorithm, which follows the problem solving heuristic of making the locally optimal choice at each stage with the hope of finding a global optimum. In particular, the method starts with no attributes and adds attributes depending on an evaluation criteria.The individual predictive ability of each feature along with the degree of redundancy between them have been chosen as the evaluation criteria, so that subsets of features or attributes that are highly correlated with the class are preferred.

The best attribute subset has been obtained for each of the six sets with a best subset attribute selection algorithm [Hall 1999]. By comparing the common and non common selected attributes, the correlated attributes can be rejected and the most important are kept. The list of the selected attributes is shown in table III.

The most important attributes are: entropy, L_5L_5 average ($\mu_{L_5L_5}$), E_9L_9 average (μ_{E9L9}) and R_9L_9 standard deviation (σ_{R9L9}). Entropy is high in an homogeneous scene and low in an inhomogeneous scene, L_5L_5 is similar to a Gaussian kernel, so the convolution of a patch with this kernel blurs the input subimage, mixing the corresponding gray values. Moreover, E_9L_9 and R_9L_9 kernels compute texture filters that react to texture in different ways so that the PO is easier to identify.

From these attributes, six LMT models for the six datasets are trained. The pairs are used to validate the models by testing one dataset in the trained model pair. The results of these tests are shown in tables IV, V and VI. Notice that in these tables the number of correctly classified instances is almost the same when the test datasets are changed for the same train set. The addition of examples also drops about a 5% the result, as the mixed images are more difficult to classify, as mentioned in section 2.3. But these numbers confirm that the addition of mixed images, where posidonia and sand appear together, does not cause an important misclassification error. So the chosen models are A', B' and C', as they contain more examples with the same ability to classify correctly. The results of the 10 fold cross-validation for A', B' and C' models can be seen in table VII.

4. EXPERIMENTAL RESULTS

Once the three models have been trained, test datasets can be used to verify the classification rates. These datasets are composed of new images which will also be preprocessed like the training images. However the patches will overlap in order to obtain a refined classification result. For A' the patch size was $25 \times 25\ px$, and the overlap has been defined as half the size of the patch: $12\ px$. The same operation is made with the other two sizes. For instance, the classification results of figure 5 are the three images in figure 10.

Table IV. Model A cross training results. Number of correctly classified instances.

Train \ Test	A	A'
A	97,07%	93,73%
A'	97,10%	93,74%

Table V. Model B cross training results. Number of correctly classified instances.

Train \ Test	B	B'
B	98,87%	95,94%
B'	98,70%	95,77%

Table VI. Model C cross training results. Number of correctly classified instances.

Train \ Test	C	C'
C	99,30%	96,75%
C'	99,30%	96,58%

An image cannot be classified entirely as belonging exclusively to one class (100% or 0% PO) since there may be intermediate levels of posidonia in there. Also, it is interesting to consider this approach as the classifier could be used to generate PO maps of the surveyed area. To this end, the overlapping results in a new kind of output classification. The classified images have light grey colored patches where the classification has resolved that this particular patch is PO. In the case that the classifier resolves that it is not PO, the resulting image remains white. As the patches overlap, the color becomes darker until it is totally black. For a central patch, up to four overlaps can occur. This results in four levels of PO in a quarter patch: 0%, 33%, 66% and 100% PO confidence. In case the overlap was defined in a different size (for example, instead of taking subimages each 12 pixels when 25×25 patch size is used, the subimages were taken at each pixel) the resulting gray levels would be smoother than only with four.

This overlap is different at the corners of the image, where there are parts of the resultant classification image that are only looked up by one patch. In these cases, the full patch has been considered to be all PO if the corresponding patch was classified in PO class or 0% PO if it belonged to the other class. This way the corners are either white or black, with no gray levels laying between them.

These models are now tested on a new dataset containing 50 PO images and 50 non PO images from the same photography database of Palma Bay. The results will be first presented in terms of image classification, and then in terms of subimage classification. This way, the correctly classified ratio as well as the false positive or the false negative rate will be different, but will allow the lecturer to appreciate how the classification process works.

The test images are known a priori, there are 50 which contain PO exclusively and 50 that do not. This particular knowledge allows the classification process to test not only the behaviour and the

Table VII. Evaluation of the trained models by 10 fold cross-validation.

Properties	A' Model	B' Model	C' Model
Instances	39000	9750	4000
Corr. Class. Instances	93,84%	95,68%	96,33%
FP rate	5,69%	5,42%	5,10%
FN rate	6,74%	3,44%	2,55%

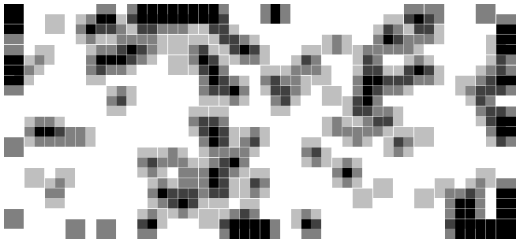

(a) Model A'.

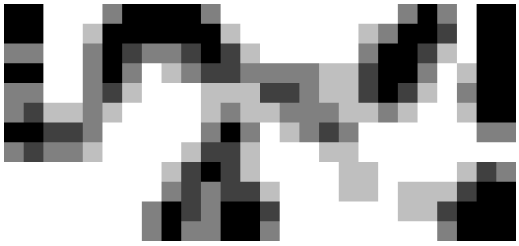

(b) Model B'.

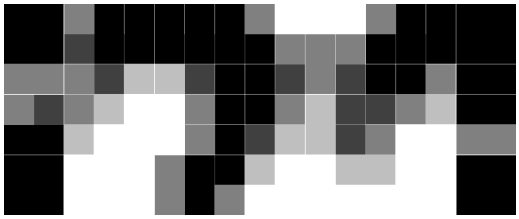

(c) Model C'.

Fig. 10. Classification results of the different models.

Table VIII. Evaluation of the tested models.

Properties	A' Model	B' Model	C' Model
Instances	107800	27500	9600
Corr. Class. Instances	98,71%	99,36%	99,55%
FP rate	2,21%	1,24%	0,88%
FN rate	0,38%	0,04%	0,02%

correctness of the classifier at a subimage level but also to have a global perspective at the whole image. The results of the classification of this database with the three models can be seen in table VIII. Note that the correctly classified instance percentage increases with the patch size, like the original model did when it was trained. This indicates that the C' model classifies better than A'. The results can be also seen at each image. In figure 11 the different classification result is plotted for each non PO image and for the different models, and in figure 12 the remaining 50 PO images are also shown.

In the figure 11 the classification results for all class 0 (not PO) images are presented, and in figure 12 there are the classification

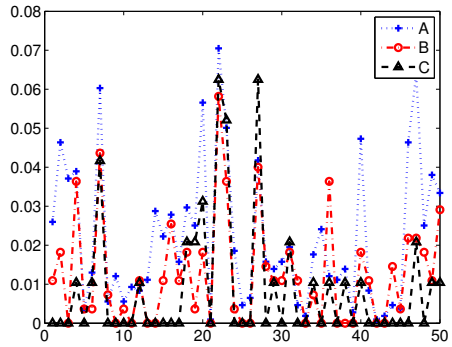

Fig. 11. Classification results of 50 non PO images.

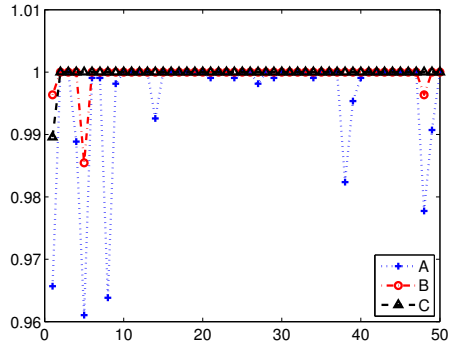

Fig. 12. Classification results of 50 PO images.

results for class 1 (PO). Those classification results lead directly to a clear classification in PO or in not PO, but when it comes to patch classification, the rates are different. In fact, the classification results shown in table VIII are patch results.

5. CONCLUSION & FUTURE WORK

The results presented in section 4 show that the classifier not only classifies correctly but also with a low false positive and false positive rate. The FP and FN rates in the experimental results are lower than in the training process. This could be due to the mixed images, where the PO and the sand are both often captured in a patch. The classifier has been trained to output a binary value when the input image is not posidonia (Class 1) or not posidonia (Class 0). Although this is a mistake, the final error in terms of classification is low, as has been seen in the table VII, and the classification is faster and simpler than if a lineal output model had been considered. Furthermore, the overlapping patches have allowed to output a set of four values of PO presence in the image.

Also the best classifier model has been chosen given the particularities of these images using Greedy stepwise method [Cormen et al. 2001] in Weka, where LMT has been chosen. Moreover, the 314 possible attributes provided have been reduced up to four of them, fast and easy to calculate given an input image. The reduction has been done using a best subset algorithm provided also by Weka.

As future work, more than two classes should be considered, taking into account different algae species, rocks, and sand. Also, the

acquisition of new images with better quality is necessary, as the ones used have noise coming from the analog readings transmitted through the underwater cable to the PC.

This work has been submitted in April 10th, accepted in May 6th, and presented in OCEANS'13 MTS/IEEE Conference in Bergen, Norway in June 13th, 2013.

APPENDIX

A. LAWS' TEXTURE ENERGY MEASUREMENTS

The figures 6(c) and 6(f) are convolved with the 25 different Laws' TEM and shown in figures 13 and 14. Dark blue is zero and dark red is one. As the value grows, the colors turns light blue, yellow, and finally red.

ACKNOWLEDGEMENTS

The authors would like to thank *Instituto Mediterráneo de Estudios Avanzados* (IMEDEA) for providing all the underwater images used in this work.

REFERENCES

ARDIZZONE, G., BELLUSCIO, A., AND MAIORANO, L. 2006. Long-term change in the structure of a Posidonia oceanica landscape and its reference for a monitoring plan. *Marine Ecology 27,* 4 (Dec.), 299–309.

CORMEN, T. H., LEISERSON, C. E., RIVERST, R. L., AND STEIN, C. 2001. *Introduction to Algorithms.* MIT press.

DIAZ-ALMELA, E., MARBÀ, N., AND DUARTE, C. M. 2007. Consequences of Mediterranean warming events in seagrass (Posidonia oceanica) flowering records. *Global Change Biology 13,* 1 (Jan.), 224–235.

FORNES, A., BASTERRETXEA, G., ORFILA, A., JORDI, A., ALVAREZ, A., AND TINTORE, J. 2006. Mapping posidonia oceanica from IKONOS. *ISPRS Journal of Photogrammetry and Remote Sensing 60,* 5 (Aug.), 315–322.

GONZÁLEZ-CORREA, J. M., BAYLE, J. T., SÁNCHEZ-LIZASO, J. L., VALLE, C., SÁNCHEZ-JEREZ, P., AND RUIZ, J. M. 2005. Recovery of deep Posidonia oceanica meadows degraded by trawling. *Journal of Experimental Marine Biology and Ecology 320,* 1 (June), 65–76.

HALL, M. 1999. Correlation-based feature selection for machine learning. Ph.D. thesis, Department of Computer Science, University of Waikato.

HALL, M., FRANK, E., HOLMES, G., PFAHRINGER, B., REUTEMANN, P., AND WITTEN, I. H. 2009. The weka data mining software: An update.

HARALICK, R., SHANMUGAM, K., AND DINSTEIN, I. 1973. Textural features for image classification. *Systems, Man and Cybernetics, IEEE Transactions on SMC-3,* 6, 610–621.

LANDWEHR, N., HALL, M., AND FRANK, E. 2005. Logistic model trees. *Machine Learning*, 1–54.

MARCH, D., ALÓS, J., CABANELLAS-REBOREDO, M., INFANTES, E., AND PALMER, M. 2013. Probabilistic mapping of Posidonia oceanica cover: A Bayesian geostatistical analysis of seabed images. *Aquatic Botany 106*, 14–19.

MATARRESE, R. AND ACQUARO, M. 2008. Applications of Remote Sensing Techniques for Mapping Posidonia Oceanica Meadows. *Geoscience and Remote Sensing Symposium, 2008. IGARSS 2008. IEEE International*, 906–909.

PASQUALINI, V., PERGENT-MARTINI, C., PERGENT, G., AGREIL, M., SKOUFAS, G., SOURBES, L., AND TSIRIKA, A. 2005. Use of SPOT 5 for mapping seagrasses: An application to Posidonia oceanica. *Remote Sensing of Environment 94,* 1 (Jan.), 39–45.

PIAZZI, L., ACUNTO, S., AND CINELLI, F. 2000. Mapping of Posidonia oceanica beds around Elba Island (western Mediterranean) with integration of direct and indirect methods. *Oceanologica acta 23*, 339–346.

SCARADOZZI, D., CONTE, G., DE CAPUA, G., SORBI, L., LUCIANI, C., DE CECCO, P., AND SORCI, A. 2009. Innovative technology for studying growth areas of Posidonia oceanica. *2009 IEEE Workshop on Environmental, Energy, and Structural Monitoring Systems*, 71–75.

SICCARDI, A., BOZZANO, R., AND BONO, R. 1997. Seabed vegetation analysis by a 2 MHz sonar. *Oceans '97. MTS/IEEE Conference Proceedings 1*, 344–350.

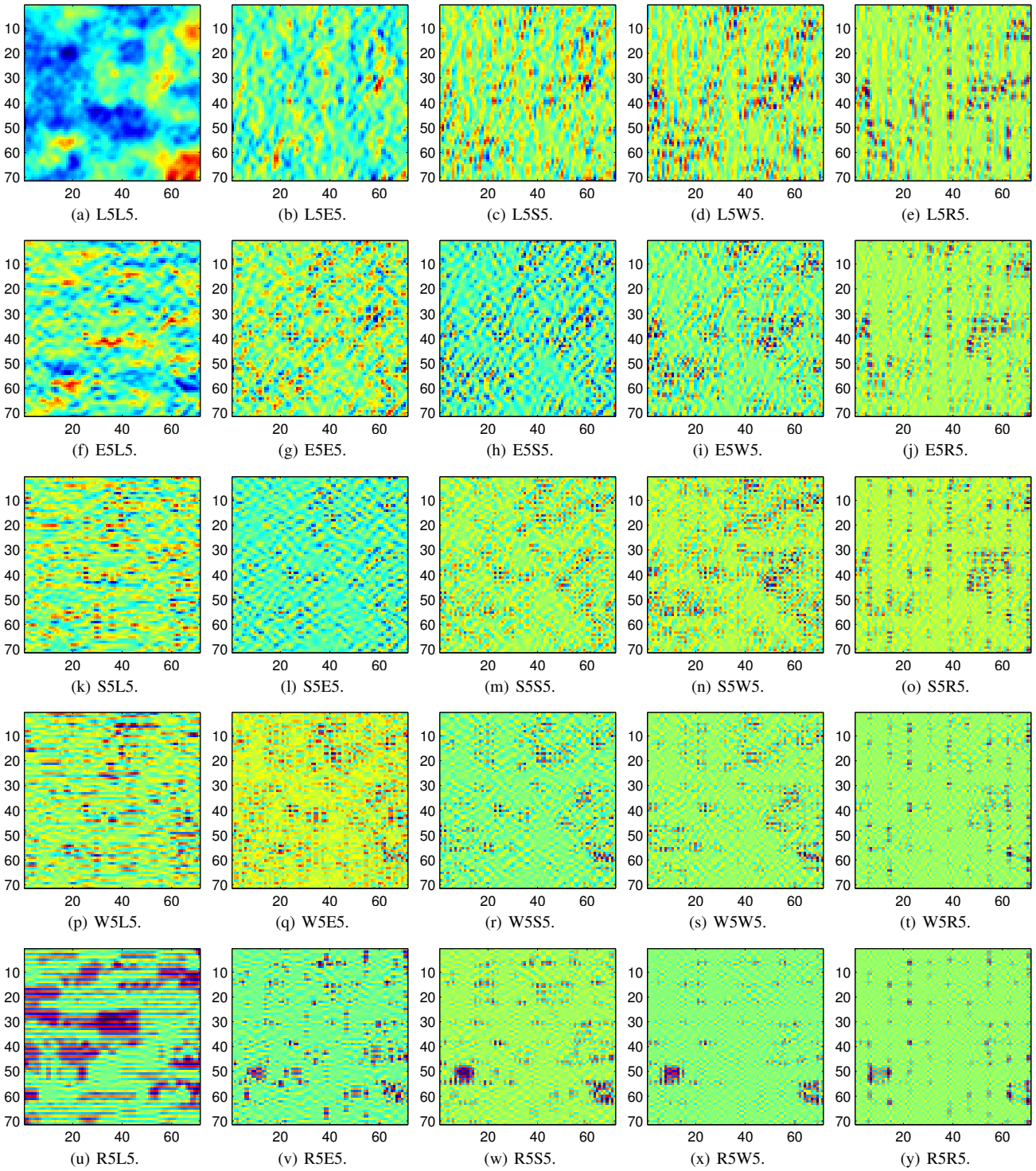

(a) L5L5. (b) L5E5. (c) L5S5. (d) L5W5. (e) L5R5.

(f) E5L5. (g) E5E5. (h) E5S5. (i) E5W5. (j) E5R5.

(k) S5L5. (l) S5E5. (m) S5S5. (n) S5W5. (o) S5R5.

(p) W5L5. (q) W5E5. (r) W5S5. (s) W5W5. (t) W5R5.

(u) R5L5. (v) R5E5. (w) R5S5. (x) R5W5. (y) R5R5.

Fig. 13. Result of the convolution of the 25 different Laws' TEM with the image in the figure 6(c).

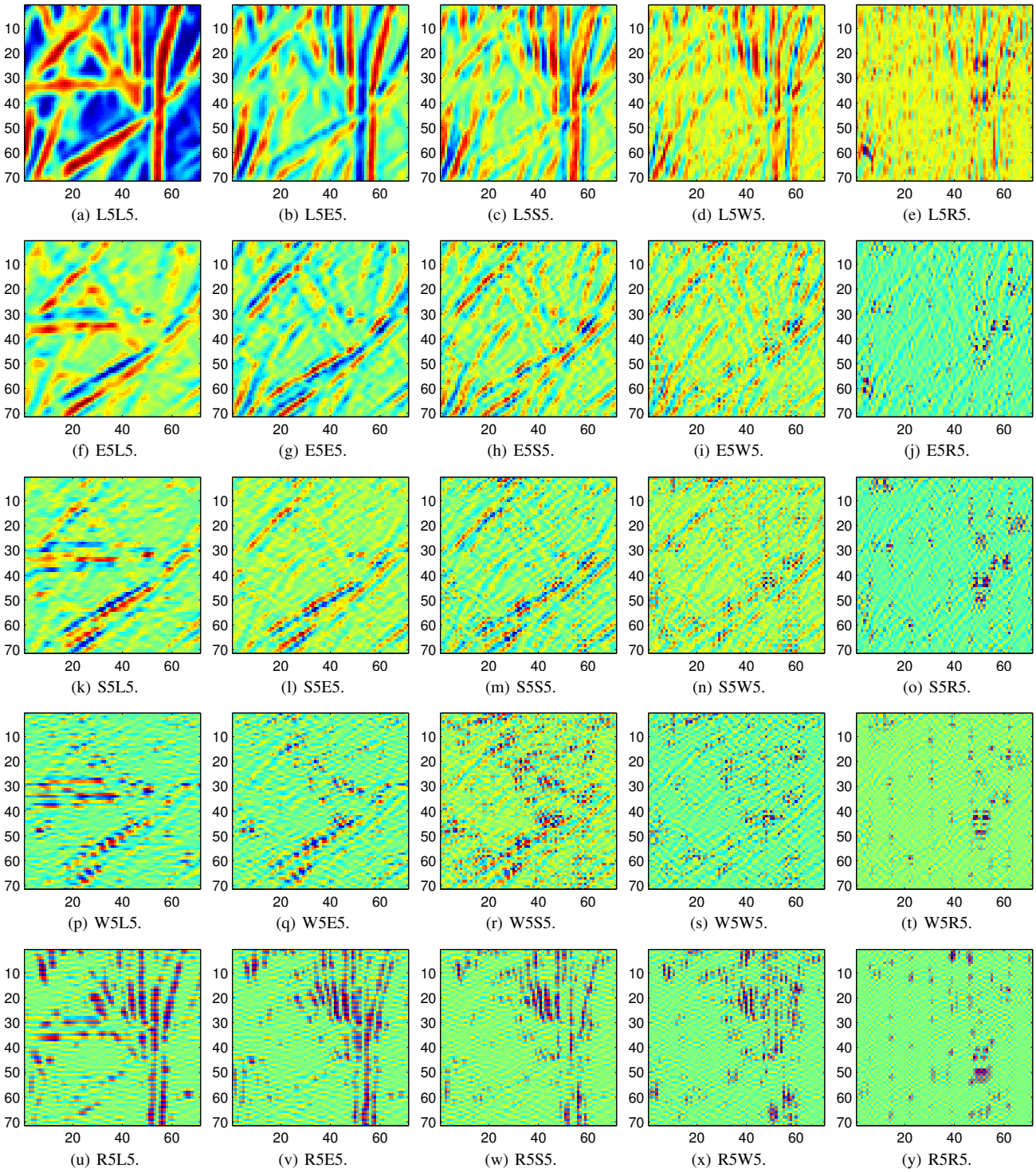

(a) L5L5. (b) L5E5. (c) L5S5. (d) L5W5. (e) L5R5.

(f) E5L5. (g) E5E5. (h) E5S5. (i) E5W5. (j) E5R5.

(k) S5L5. (l) S5E5. (m) S5S5. (n) S5W5. (o) S5R5.

(p) W5L5. (q) W5E5. (r) W5S5. (s) W5W5. (t) W5R5.

(u) R5L5. (v) R5E5. (w) R5S5. (x) R5W5. (y) R5R5.

Fig. 14. Result of the convolution of the 25 different Laws' TEM with the image in the figure 6(f).